Chinese Chemical Letters 37 (2026) 111548

Contents lists available at ScienceDirect

Chinese Chemical Letters

journal homepage: www.elsevier.com/locate/cclet

Multidimensional host-guest molecule screening *via* 96-well plate assays to facilitate the development of natural product nanomicelles

Wenzheng Li[a], Ke Zhang[a], Wenjing Liu[b], Ting Li[a], Wei Li[a], Lijuan Wu[a], Maodong Wang[a], Hangyun He[a], Pengfei Tu[a,*], Yuelin Song[a,*]

[a] *Modern Research Center for Traditional Chinese Medicine, Beijing Research Institute of Chinese Medicine, Beijing University of Chinese Medicine, Beijing 102401, China*
[b] *School of Pharmacy, Henan University of Chinese Medicine, Zhengzhou 450046, China*

ARTICLE INFO

Article history:
Received 17 March 2025
Revised 27 May 2025
Accepted 5 July 2025
Available online 7 July 2025

Keywords:
Bile acid-lecithin nanomicelles
Host-guest complex screening
Natural products
Anti-inflammation
Muscone

ABSTRACT

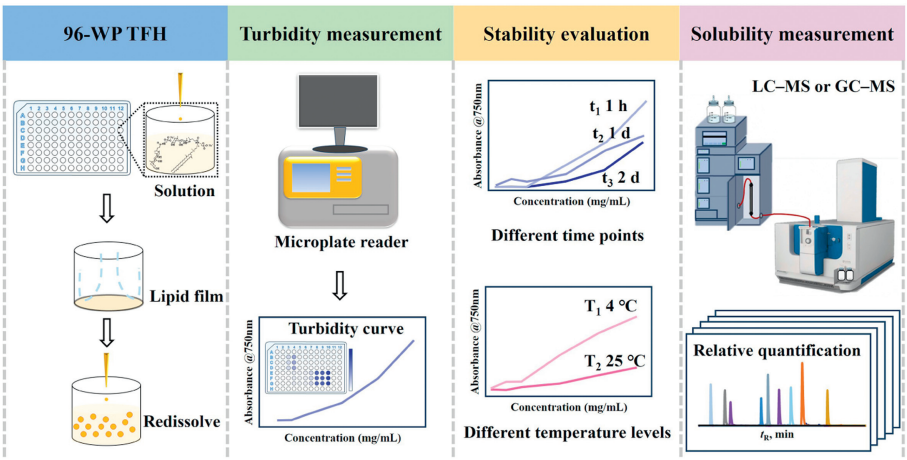
Nanomedicine preparation is a promising approach for the effective utilization of natural bioactive products. However, the successful fortification of natural products into nanocarriers in a host-guest manner remains a great challenge. Here, a 96-WP TFH/TM strategy integrating 96-well plate mediated thin-film hydration, turbidity measurement, stability evaluation, and relative quantification, was proposed to screen host-guest complexes. As a proof-of-concept, biomimetic bile acid-lecithin nanomicelles (BA-L NMs) were used as nanocarriers and 51 natural products were assayed for guest molecules. Muscone came out as the fit-for-purpose candidate to produce stable NMs, namely M-NMs. Following spectroscopic characterization and molecular dynamics calculation, hydrophobic interactions, hydrogen bonding, and salt bridges were demonstrated as the primary correlations amongst taurocholic acid, lecithin, and muscone. M-NMs exhibited significant *in vitro* and *in vivo* anti-inflammation features. Together, we developed a 96-WP TFH/TM strategy to achieve high-throughput host-guest complex screening, facilitating the development of natural product nanomicelles.

© 2025 Published by Elsevier B.V. on behalf of Chinese Chemical Society and Institute of Materia Medica, Chinese Academy of Medical Sciences.

Natural products are a valuable source of lead compounds and potential drug candidates due to their diverse chemical structures and great biological activities [1,2]. However, a number of natural products suffer from poor solubility and low bioavailability, extensively dampening their applications and investigations [3]. Hitherto, nanocarriers occupy a hotspot in drug delivery field [4–8]. The sub-100 nm particles can significantly enhance the stability and solubility of pharmaceutical compounds. These characteristics not only promote efficient cellular internalization but also extend circulatory half-life, thereby enhancing both bioavailability and safety [9]. Several successes have been reached for natural products delivery using nanocarriers, such as liposomes for ammonium glycyrrhizate skin delivery [10]. However, the existing nanoparticle exploration strategies rely heavily on trial-and-error approaches or empirical optimization. Because the carrying capacity and stability of nanocarriers are determined by the host-guest molecule interactions [11], extensive screening, optimization, and stability investigation, successively, are extremely important. Conventional screening workflows are typically driven by the observation of nanoparticles through Tyndall effect detection or size measurement by dynamic light scattering (DLS). Upon confirmation of their presence, subsequent steps usually involve isolating the nanoparticles and characterizing their morphology, component composition, stability, and so forth [12]. However, these methods are limited to sequential sample analysis, leading to low throughput and requiring relatively large sample volumes (0.5–1 mL). More advanced techniques, such as scanning electron microscope (SEM) or other electron microscopes can be used directly to observe the presence of nanoparticles [13]. Nuclear magnetic resonance (NMR) spectroscopy also provides a method to investigate guest loading [11]. Native mass spectrometry (nMS) has emerged as a promising technique for micelle and nanodisc characterization [14,15], providing simultaneous structural identification and quantitative analysis of nanoparticles. However, these methods require expensive equipment, resulting in high costs and not user-friendly. Although *in silico* approaches exactly facilitate rapid screening of the self-assembly ability of candidate drug molecules through outputting theoretical results [16,17], the complexity of reality surpasses computational predictions. The development of a high-throughput, cost-effective, and user-friendly host-guest molecule screening method is of utmost urgency.

* Corresponding authors.
E-mail addresses: pengfeitu@bjmu.edu.cn (P. Tu), syltwc2005@163.com (Y. Song).

https://doi.org/10.1016/j.cclet.2025.111548
1001-8417/© 2025 Published by Elsevier B.V. on behalf of Chinese Chemical Society and Institute of Materia Medica, Chinese Academy of Medical Sciences.



Scheme 1. Schematic workflow of the 96-well plate-based screening platform for host-guest molecular interactions. The integrated procedure involves four sequential phases: (1) 96-well plate-based thin-film hydration (96-WP TFH), including dissolution of bile acid, lecithin, and hydrophobic natural products in organic solvent, solvent evaporation to form thin films, and hydration with aqueous solvent; (2) turbidity measurement at 750 nm using a microplate reader; (3) stability evaluation by measuring turbidity at different time points as well as multiple temperature levels; (4) relatively quantitative measurements by LC–MS or GC–MS.

During lead natural products screening, the utilization of 96-well plates (96wp) extensively occurs because of the high-throughput and user-friendly advantages. Hence, the implementation of the widely popular method for nanomicelles (NMs) or liposomes preparation, thin-film hydration in 96wp, should be feasible and theoretically convenient to complete the screening task. However, assessing the formation of NMs with conventional methods may be challenging due to the difficulty in observing the Tyndall effect or measuring nanoparticle size *via* DLS in a 96-well plate. The final step of 96wp assays generally involves the absorption wavelength determination using a microplate reader, and fortunately, such step enables convenient turbidity measurements. The turbidity of the solution, commonly deployed as an indicator for nanoparticle aggregation, can offer a quantitative reflection of the concentration or particle size of the suspended particulate matter. In general, greater turbidity values correspond to larger particle sizes or higher concentrations, and *vice versa* [18]. Theoretically, the turbidity of hydrophobic drugs will be significantly reduced when they are solubilized and encapsulated in nanocarriers compared to being dispersed in aqueous medium. Therefore, the host-guest complex screening might be accomplished *via* 96wp assays.

Here, a strategy integrating thin-film hydration, turbidity measurement, stability evaluation, and relative quantification in 96wp, was proposed to screen host-guest complexation. As a proof-of-concept, biomimetic bile acid-lecithin nanomicelles (BA-L NMs) bearing biocompatible and biodegradable merits served as the host nanocarriers [19,20]. A total of 51 natural bioactive products, encompassing flavonoids, alkaloids, coumarins, terpenes, quinonoids, and others, were evaluated for guest molecules. Muscone, a natural product featured by the anti-inflammatory property [21,22], as a representative guest molecule forming stable muscone NMs (M-NMs) was chosen to in depth explore the interaction mechanisms. Thereafter, several preliminary investigations were conducted to evaluate the anti-inflammatory activities of M-NMs for dermal delivery. Collectively, the obtained findings are envisioned to demonstrate the 96wp assays as a promising approach for screening host-guest molecule interactions and subsequently facilitating the design of natural product nanomicelles.

The entire workflow was conducted in a 96-well plate by performing four progressive steps: (1) 96wp-based thin-film hydration (96-WP TFH), briefly, consisting of three successive experiments such as dissolving bile acid (BA), lecithin (L), and hydrophobic natural products in organic solvent, evaporating the organic solvent, and hydrating NMs with aqueous solvent (normal saline in the current study); (2) turbidity measurement at 750 nm using a microplate reader; (3) stability evaluation by measuring turbidity at different time points as well as multiple temperature levels; and (4) relatively quantitative measurements by LC–MS or GC–MS (Scheme 1). All 51 hydrophobic natural bioactive products (Tables S1 and S2 in Supporting information) were screened as guest molecule candidates to justify the applicability of 96-WP TFH/TM strategy. Direct dispersion of each candidate in normal saline acted as the negative control, while BA-L NMs played the role of the guest molecule-free control. To simultaneously achieve effective solubilization for hydrophobic guest molecules and to form stable nanoparticles, the resultant NMs should fulfill the following two prerequisites. Firstly, the turbidity exhibited a significant decrement compared to the negative control, and nonetheless, being comparable with that of the natural product-free control. Secondly, the turbidity value should maintain stable over a relatively long period at different temperature levels.

We initially attempted to construct NMs through employing the extensively utilized bile acids and lecithin, such as sodium taurocholate (NaTCA) and yolk lecithin, respectively, at a fixed proportion (BA:L = 10:3). Subsequently, we systematically augmented the amount of hydrophobic guest molecules to assess turbidity [23]. As a result, the addition of BA-L NMs led to a significant turbidity decrement for resveratrol, isoliquiritigenin, licochalcone A, or muscone, compared to the respective negative control, even reaching a clear and transparent status (Fig. 1A and Fig. S1 in Supporting information). Moreover, significant turbidity variation did not occur for isoliquiritigenin, licochalcone A, or muscone at different temperatures or time points, indicating the successful entry of guest molecules into the carriers.

The encapsulation of guest molecules in BA-L NMs was further validated through relatively quantitative analysis. Four volatile components, including borneol, menthone, β-elemene, and muscone, were quantitatively analyzed using GC–MS (Table S1), while others were monitored by LC–MS (Table S2 and Fig. S2 in Supporting information). As a result, BA-L NMs demonstrated the enhanced solubilization efficacy, and particularly, more than two-fold solubility improvement occurred for the high-concentration groups belonging to 23 bioactive compounds, comprising 11 flavonoids, 3 terpenoids, 3 alkaloids, and 6 other natural products. Notably, isoliquiritigenin, licochalcone A, and muscone exhibited excellent

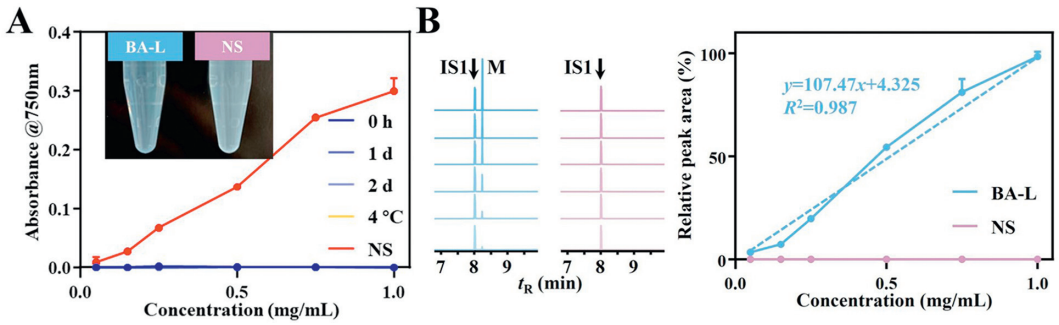


Fig. 1. Host-guest molecule interaction screening with 96wp assays. (A) Turbidity measurements at various concentrations, temperatures, and time points using muscone as a representative example. (B) Relative quantitation of the solubilizing compound and linear regression ($y = 107.47x + 4.325$, $R^2 = 0.987$ for muscone). IS1: internal standard 1, M: muscone, NS: normal saline.

solubility as aforementioned (Fig. 1B and Fig. S3 in Supporting information). Representatively, muscone was totally insoluble in normal saline because it was almost undetectable when being dispersed in normal saline. However, following the addition of BA-L NMs, the relative peak areas of muscone exactly showed a linear increment with the fortified amounts ($y = 107.47x + 4.325$, $R^2 = 0.987$), even being comparable with the values of those serial standard solutions (Fig. 1B). Similar results were also observed for either isoliquiritigenin or licochalcone A (Fig. S3). The natural products whose turbidity decreased and/or solubility increased were summarized in Fig. S4 (Supporting information). Moreover, the well-defined approaches, such as Tyndall effect evaluation and DLS-based particle size measurement were jointly employed to consolidate the results. As expected, the results exactly justified the aforementioned findings (Fig. S5 in Supporting information).

To further confirm the utility of 96-WP TFH/TM, we assessed the detection limits and linear correlations between turbidity and particle size for the micelles corresponding to muscone. The results demonstrated that even undergoing 16-fold dilution, the turbidity of three distinct samples were still detectable and the detection limit came out as low as 0.5 mg/mL (Fig. S6A in Supporting information). Moreover, the linear relationships between dilution ratio and turbidity confirmed that greater concentrations of nanoparticles exactly corresponded to higher turbidity level. Further, we also observed the linear correlations between nanoparticle size and turbidity (Fig. S6B in Supporting information). Thereafter, comparisons were conducted for 96-WP TFH/TM against frequently used approaches such as DLS and Tyndall effect measurements (Table S3 in Supporting information). The 96wp assay offers a high-throughput, cost-effective, and user-friendly screening platform for host-guest complexes with three key advantages. (1) Parallel analysis of dozens of samples significantly increases throughput compared to the traditional methods. The screening of 51 natural products, encompassing varied formulations and replicated experimental designs, generated approximately 1 000 testing samples and merely cost about 20 min using the novel methodology, whilst DLS only assayed less than ten samples within the equivalent time. (2) The new approach was advantageous at minimizing sample and solvent consumption ($\leq$100 μL *vs.* about 1000 μL per test for DLS/Tyndall characterization), with further achievable reductions through applying 384-/1536-well plate assays, exactly meeting the green chemistry principles. (3) Similar to Tyndall effect analysis, the 96-WP TFH/TM operation required minimal technical expertise and was designed with user-friendly feature. This integrated approach enabled rapid, economical large-scale screening in addition to maintaining experimental precision, representing a methodological advancement in molecular interaction studies. The proportion amongst BA, lecithin, and muscone was optimized in a progressive manner using 96wp assays. The results demonstrated a synergistic decrement in the turbidity of muscone by BA and lecithin, with an optimal proportion for BA against L within 15:(5∼15) (Fig. S7 in Supporting information).

Consequently, the above findings suggested that muscone, isoliquiritigenin and licochalcone A should be the suitable guest molecules for BA-L NMs, and 96wp assays were a superior approach for host-guest complex screening and even for formulation optimization. Due to its exceptional properties as a guest molecule in the formation of NMs with BA and L and its anti-inflammatory properties, muscone was selected as a representative for further investigation.

We preliminarily assessed the synergistic action between BA and lecithin towards facilitating muscone solubilization. The optimal ratio came out as BA:L:muscone = 15:(8–10):(14–18) mmol/L using 96-WP TFH/TM strategy. The validity of these findings was further substantiated through measuring the size and polydispersity index (PDI) by DLS analysis (Fig. S8 in Supporting information). The central composite design (CCD) response surface method was employed for further optimization to obtain NMs with reduced dimensions and enhanced uniformity. The molar concentration of lecithin (X_1) and the theoretical molar concentration of muscone (X_2) were considered as independent variables, while particle size (Y_1) and PDI (Y_2) served as the dependent variables (Table S4 in Supporting information) [24]. The obtained regression equations were as $Y_1 = 108.6261 - 21.7760X_1 - 0.8626X_2 - 0.3850X_1X_2 + 1.4924{X_1}^2 + 0.1833{X_2}^2$ ($R^2 = 0.9794$, $F = 66.40$, $P < 0.0001$), indicating statistical significance with a non-significant lack of fitting value ($P = 0.1478 > 0.05$), and $Y_2 = 5.9666 - 1.4337X_1 + 0.0574X_2 + 0.0022X_1X_2 + 0.0777{X_1}^2 - 0.0015{X_2}^2$ ($R^2 = 0.9521$, $F = 27.81$, $P = 0.0002 < 0.05$), suggesting good fitting without significant lack of fitting value ($P = 0.2315 > 0.05$). These equations demonstrated excellent fitting and predictive capabilities. Three-dimensional response surface and contour maps are shown in Fig. 2A and Fig. S9 (Supporting information), respectively. For convenient operation, the final optimized ratio for BA:L:muscone was fixed at 15:9:15 mmol/L. Except NaTCA, other commonly utilized BAs including sodium cholate (NaCA), sodium glycine cholate (NaGCA), sodium glycochenodeoxycholate (NaGCDCA), and sodium taurodeoxycholate (NaTDCA) were evaluated for the fabrication of NMs. All BAs were able to form NMs with L and advance muscone solubility. However, tauro-conjugated BAs demonstrated greater efficacy (Fig. S10 in Supporting information), possibly attributed to the appropriate hydrophobicity and size features [25].

According to the optimized formulation, three batches of M-NMs were prepared in parallel. NMs exhibited a distinct and transparent appearances, with a hydrodynamic size of 11.35 ± 0.66 nm and a relatively narrow size distribution (PDI as 0.147 ± 0.023), demonstrating that the optimized formulation exhibited great reliability (Fig. 2B). M-NMs showed zeta potentials around −20.0 mV

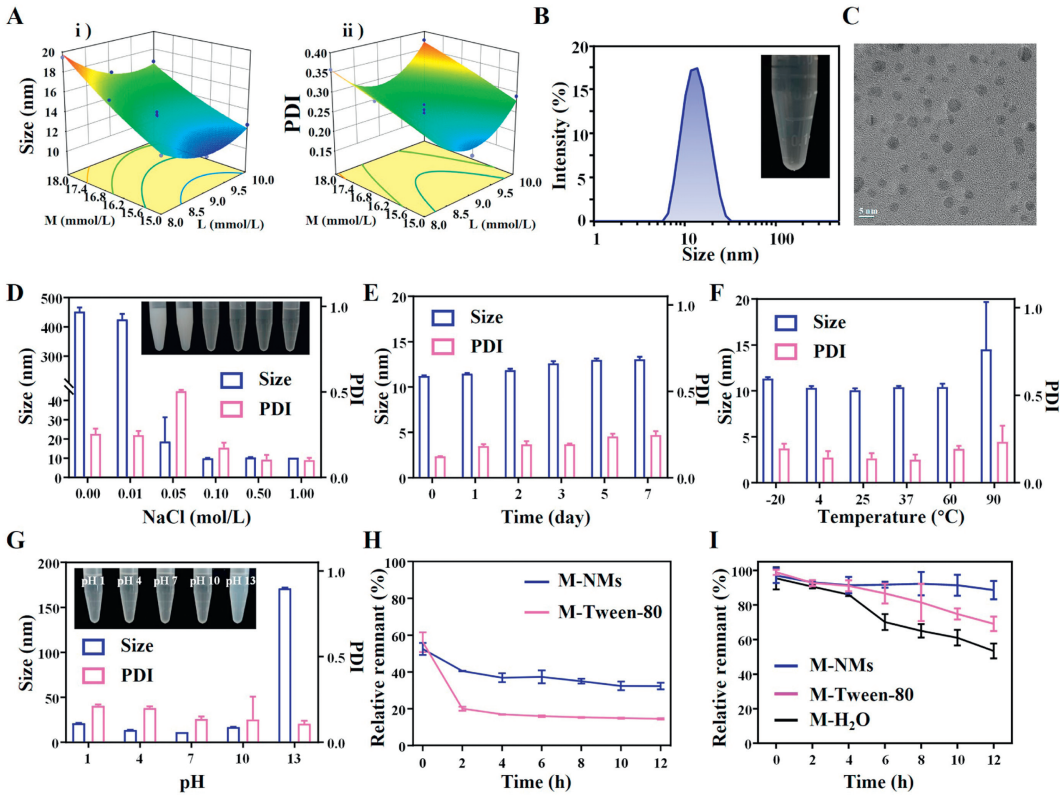


Fig. 2. Fabrication and physicochemical characterization of M-NMs. (A) 3D response surface diagram of independent variables formulas of lecithin (L) and muscone (M) and dependent variables size and PDI. (B) DLS measurement of M-NMs size. Inset: photographic image of M-NMs under daylight. (C) TEM image of M-NMs. Variations of hydrodynamic sizes and PDI of M-NMs under different NaCl concentrations (D), time points (E), temperatures (F), and pH levels (G). (H) Stability evaluation of M-NMs in DMEM. (I) Relative residual measurement of muscone after exposure to a continuous stream of air.

in phosphate buffered saline solution, corresponding to excellent aqueous stability. Transmission electron microscopy (TEM) images revealed that the micromorphology of M-NMs exhibited a non-adhesive near-spherical morphology with sizes ramping from 3 nm to 5 nm (Fig. 2C). Further, the quantitative results demonstrated that M-NMs exhibited a drug-loading rate as 13 % and encapsulation efficiency as 57 %.

Upon hydration with solutions containing different concentration levels of NaCl, both the size and size distribution decreased when NaCl concentration kept growing until 0.5 mol/L (Fig. 2D). The fortification of NaCl to aqueous NMs resulted in a time-dependent turbidity decrement, and a steady status was reached after approximately 120 min using 0.05 mol/L NaCl (Fig. S11 in Supporting information). This tendency was further consolidated at different NaCl concentration levels. When NaCl concentration reached at 0.1 mol/L, the solution immediately transferred from milky to clear status, indicating that NaCl effectively inhibited flocculation of M-NMs (Fig. S12 in Supporting information). Consequently, the stability of M-NMs could be dramatically impacted by NaCl concentration, and NMs were hydrated using 0.5 mol/L NaCl solution to advance stability.

The stability of NMs is extremely important for the clinical applications [26]. Following evaluations, significant change in term of either hydrodynamic size or size distribution within 7-day incubation was failed to occur, indicating the high-level stability feature for M-NMs (Fig. 2E). Furthermore, M-NMs exhibited remarkable stability within a wide temperature span from –20 °C to 60 °C; however, the structures were destroyed after a 2-h incubation at 90 °C (Fig. 2F). The stability was further evaluated under the simulated human status *via* varying pH values and incubation times in Dulbecco's modified eagle medium (DMEM) solution [27]. As a result, under both acidic conditions (pH 1 and 4) and mild alkaline conditions (pH 10), moderate increment was observed for either hydrodynamic size or size distribution. However, within the alkaline environment, the size was dramatically increased (Fig. 2G), indicating that M-NMs were instable in such strong alkali environment. To avoid the influence from DMEM solution, we assessed the relative remnant (RR,%) of muscone for M-NMs, through deploying the sample, namely M-Tween-80 solution that was prepared by dissolving muscone in water in the presence of Tween-80, as the control. As a consequence, RR (%) values for M-NMs showed a slight decrement upon incubation time, whereas RR (%) values for M-Tween-80 solution significantly decreased gradually within two hours, indicating the significant stability for M-NMs (Fig. 2H). Additionally, owing to the volatility property for muscone, we compared RR (%) values amongst M-NMs, M-Tween-80 solution, and muscone-H_2O dispersion after the exposure to streaming air. The results suggested that both M-NMs and M-Tween-80 were significantly superior to muscone-H_2O dispersion during the initial six hours; thereafter, only M-NMs dramatically inhibited the volatilization of muscone (Fig. 2I). Overall, the great stability of M-NMs demonstrated the potential as a promising nanomedicine.

To investigate the molecular interactions amongst BA, lecithin, and muscone, as well as to reveal the self-assembly mechanisms of M-NMs, several spectroscopic and spectrometric assays together with molecular dynamics (MD) simulation were conducted. Because lecithin sourced from egg yolk is a complex mixture of various phosphatidylcholine species, we thereby employed 1-palmitoyl-2-oleoyl-*sn*–glycero–3-phosphocholine (POPC) that is a typical species in lecithin to simplify the relevant evaluations. As shown in Fig. S13A (Supporting information), NaTCA structurally possesses hydroxyl groups orienting towards the concave side (α plane) of the carbon framework, nonetheless, exhibiting a hydrophobic convex side (β plane). Obviously, the structure was quite

different from the conventional surfactant bearing a hydrophobic tail and hydrophilic head groups, and was different from muscone exhibiting a hydrophobic scaffold as well.

TEM and DLS measurement results also demonstrated that it was appropriate to employ POPC as a representative for lecithin (Fig. S13B in Supporting information). UV–vis spectrum exhibited only terminal absorption peak for BA. Upon the addition of lecithin ranging from 0 mmol/L to 9 mmol/L, a red shift was observed; however, none such shift was observed for the further addition (Fig. S13C in Supporting information). Moreover, the further increment of muscone was failed to initiate any spectra shift when maintaining the proportion of NaTCA:POPC at 15:9 (mmol/L), indicating that muscone did not significantly impact the structure of BA-L NMs. FT-IR assay revealed that M-NMs exhibited similar structural features with monomer molecules (Fig. S13D in Supporting information). However, due to the absence of distinctive characteristic peaks, UV–vis and FT-IR spectral information was not able to provide pronounced clues for the molecular interactions within M-NMs.

^{1}H NMR and NOESY spectroscopic assays were then performed to gain more structural insights into M-NMs [28,29]. Concerning NaTCA, the chemical shifts of H-18 (from 0.627 to 0.617 ppm, $\Delta\delta = -0.010$ ppm), H-19 (from 0.832 to 0.812 ppm, $\Delta\delta = -0.020$ ppm), and H-7α (from 3.810 to 3.793 ppm, $\Delta\delta = -0.017$ ppm) were significantly reduced, while the chemical shift growth occurring for H-21 (from 0.930 to 0.960 ppm, $\Delta\delta = 0.030$ ppm) and H-26 (from 3.008 to 3.016 ppm, $\Delta\delta = 0.008$ ppm) indicated the chemical environment change (Fig. 3A). The occurrences of H-18, H-19, and H-21 on the β plane of NaTCA (Fig. S13A) served as the pronounced evidence for the hydrophobic interaction between NaTCA and POPC, which was exactly consistent with previous findings [30–32]. The chemical shift pattern of the protons in M-NMs did not show significant changes compared to NaTCA-POPC NMs, except for the alkane chain of POPC (from 1.196 ppm to 1.209 ppm, $\Delta\delta = 0.013$ ppm), indicating an obvious interaction between POPC and muscone molecules (Fig. 3A). NOESY analysis further showed the correlations between 2-H_a, 2-H_b, and 15-H_2 of muscone with the alkane chain of POPC (Fig. 3B), suggesting significant hydrophobic interactions between POPC and muscone. However, none additional intramolecular interaction was observed between POPC and muscone. The similarity of ^{1}H NMR spectra between NaTCA-POPC NMs and M-NMs was fully consistent with the findings from UV–vis spectrum comparison. Above all, muscone did not significantly affect NaTCA-POPC NMs structure, and we tentatively regarded that M-NMs should inherit NaTCA-POPC NMs structure.

Electrospray ionization (ESI)-MS usually facilitates the generation of highly charged molecules and noncovalently bound molecular complexes, thereby enabling the investigation of intermolecular interactions in a comprehensive manner [33,34]. In the low mass scale (m/z 150–1000), as expected, the signals belonging to the monomers of muscone ($[muscone+H]^+$, m/z 239.24), TCA ($[TCA+H]^+$, m/z 516.30, $[TCA+Na]^+$, m/z 538.28, and $[NaTCA+Na]^+$, m/z 560.26), and POPC ($[POPC+H]^+$, m/z 760.58 and $[POPC+Na]^+$, m/z 782.57) in positive ionization polarity (Fig. S14A in Supporting information) and the monomer TCA ($[TCA-H]^-$, m/z 514.28) in negative ionization polarity were observed (Fig. S14B in Supporting information). Because the abundant signal intensity was observed for all compounds in the positive ion mode, our attention was primarily paid onto exploring intermolecular interactions within a high mass range (m/z 1000−3000) through deploying positive ionization polarity. The presence of ions corresponding to the oligomers, including tetramers, pentamers, and even hexamers for TCA were observed, because the hydrogen bonding interactions amongst their monomers facilitated these phenomena [35]. Similar signals were also observed for POPC (Fig. 3C and Fig. S15 in Supporting information). Additionally, higher-order aggregates were also detected. Taking oligomers at m/z 2080.43 as an example, the signal was annotated as TCA and POPC cluster ions after elemental composition calculation ($C_{110}H_{209}N_3Na_2O_{23}P_2S$). The presence of an isotopic signal bearing 0.5 Da difference indicated doubly charged state for the ion cluster (Fig. 3C) [36]. After undergoing collision induced dissociation (CID), some signals correlating to monomers and oligomers such as $[TCA+2Na-H]^+$ at m/z 560.26, $[POPC+Na]^+$ at m/z 782.57, $[2TCA+3Na-2H]^+$ at m/z 1097.54, $[TCA+POPC+2Na-H]^+$ at m/z 1319.84, and $[2PC+Na]^+$ at m/z 1542.13 appeared, further demonstrating that the precursor ion was generated from the ionized complexes of TCA and POPC, including the singly charged ion ($[TCA+2POPC+2Na-H]^+$) and the doubly charged ion ($[2TCA+4POPC+4Na-H]^{2+}$). Hence, significant interactions should occur between TCA and POPC. Because electrostatic interactions are intensified and hydrophobic forces are diminished during the transformation of micelles from a solution to a gas phase environment in ion source chamber [37,38], we plausibly hypothesized the existence of additional interactions except for hydrophobic interaction between NaTCA and POPC. Notably, no discernible aggregates were observed for muscone in the spectrum, suggesting that the primary interactions involving muscone and other molecules were dominated by hydrophobic forces. The quantitative measurement results of muscone indicated a great affinity between muscone and lecithin instead of BA, when muscone was solubilized using both BA and lecithin individually (Fig. S16 in Supporting information). This phenomenon was attributed to the hydrophobic alkyl chains of lecithin, in conjunction with other interactions reminiscent of van der Waals forces [39].

MD simulations were thereafter carried out to illustrate the self-assembly mechanisms of M-NMs. In brief, TCA, POPC, and muscone were introduced into a cubic simulation box with dimensions of 10 nm at a ratio of 20:12:10. Subsequently, the system was solvated with water containing NaCl at a concentration of 0.2 mol/L. As depicted in Fig. 4A, spontaneous aggregation of NaTCA, POPC, and muscone leads to the formation of the mixed micelles. Notably, muscone and lecithin served as the primary building blocks within the seed micelle (20 ns), while some NaTCA molecules gradually surrounded the micelles. Additionally, there were still residual free NaTCA molecules in solution due to the great water solubility. The dynamic process of self-assembly is illustrated in Fig. 4A. Furthermore, intermolecular interactions among M-NMs were also analyzed, and the results revealed not only hydrophobic interactions but also hydrogen bonds and salt bridges between NaTCA and POPC contributing to M-NMs complexation (Fig. 4B).

To further validate the intermolecular interactions within M-NMs, sodium dodecyl sulfate (SDS) and urea were separately introduced into the M-NMs. SDS was used to disrupt hydrophobic interactions within the complexes, while urea induced competitive hydrogen bonding [40]. DLS analysis demonstrated a reduction in size upon the gradual addition of SDS, suggesting the disintegration of M-NMs (Fig. 4C-i). When the concentration of SDS reached 0.5 mol/L, none particle was detected because insufficient scattering events were resulted from excessively small scattering cross sections [41]. On the contrary, gradual addition of urea led to an increment in both size and size distribution range of M-NMs (Fig. 4C-ii), suggesting the occurrence of flocculation. The incorporation of SDS and urea offered the pronounced clues for the involvement of hydrophobic interactions and hydrogen bonds, respectively.

Based on the aforementioned studies, we plausibly proposed self-assembly mechanisms of M-NMs. The details are shown in Fig. 4D. Overall, the self-assembly process of M-NMs was primarily driven by diverse noncovalent interactions. The hydrophobic interactions between lecithin, POPC as a representative, and muscone enabled the formation of lipid oligomers, while intermolecular hy-

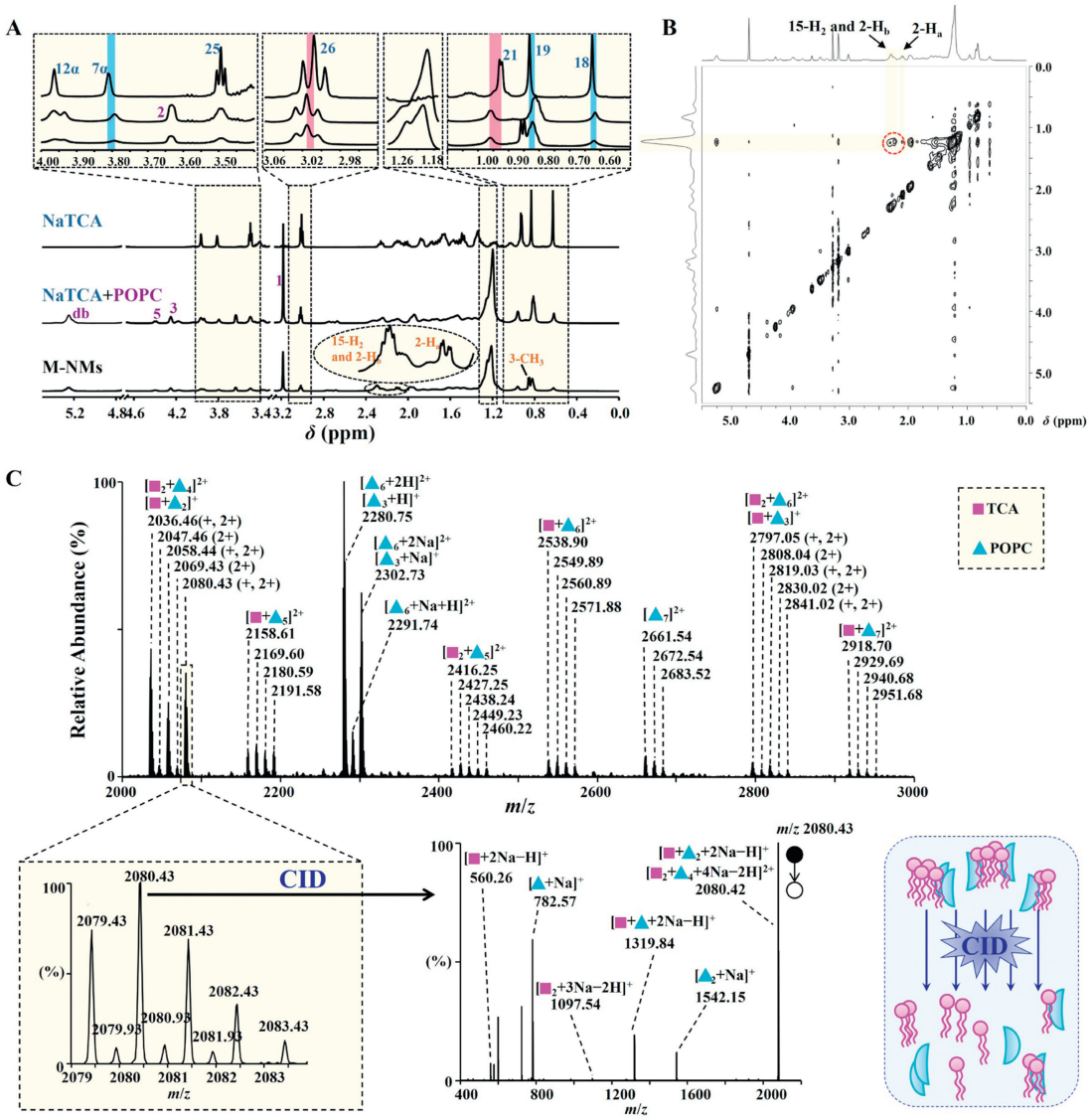


Fig. 3. Spectroscopic properties of M-NMs. (A) ^{1}H NMR spectra of NaTCA, NaTCA+POPC, and M-NMs. (B) NOESY spectra of M-NMs. (C) MS^{1} spectrum of M-NMs at *m*/*z* 2000–3000 and representative MS/MS analyses of polymer at *m*/*z* 2080.43.

drogen bonds, salt bridges, and hydrophobic interactions between BA and lecithin thereafter advanced the assembly of higher-order mixed aggregates. Subsequently, these aggregates further assembled into uniform near-spherical nano-micelles.

Lipopolysaccharide (LPS)-stimulated cells as the *in vitro* inflammation model and some swelling mice and rats as the *in vivo* inflammation models were deployed to estimate the anti-inflammatory benefits of M-NMs. As depicted in Fig. S17 (Supporting information), nitric oxide (NO) production is significantly greater ($P < 0.01$) in LPS-stimulated RAW 264.7 cells compared to untreated cells, indicating the success of modeling. Treatments with M-NMs at concentration levels of 10, 20, and 30 μmol/mL resulted in a dose-dependent reduction of NO production. The anti-inflammatory effects of M-Tween-80 solution and BA-L NMs were also assayed in parallel as controls, and as a result, either M-Tween-80 solution or BA-L NMs exhibited anti-inflammatory properties, indicating the pronounced anti-inflammatory potentials of both muscone and BA [42,43]. However, the anti-inflammatory effects of M-NMs were dramatically greater than either M-Tween-80 solution or BA-L NMs. In particular, at a concentration of 30 μmol/mL, M-NMs exhibited greater inhibition of NO production compared to M-Tween-80 and BA-L NMs with a significant difference ($P < 0.01$). This improvement in the anti-inflammatory outcomes of M-NMs on RAW 264.7 cells could be attributed to their remarkable stability in DMEM (Fig. 2H).

The transdermal route offers localized and controlled release of medicines, which may result in a consistent blood level profile, reduced systemic side effects, and greater patient compliance [44]. Therefore, we utilized pharmacological models on both mouse and rat to assess the anti-inflammatory performances of M-NMs for dermal delivery. Xylene-induced ear edema, as a widely utilized inflammation model, allows the anti-inflammatory activity assessment [45]. After xylene administration, the mice exhibited obviously inflammatory symptoms, including redness and swelling in the right ears. As depicted in Fig. S18 (Supporting information), there is a significant increment in ear edema by 137 % ($P < 0.01$). However, M-NMs demonstrated a dose-dependent inhibitory effect on ear edema (10 mg/kg: $P < 0.05$; 15 mg/kg: $P < 0.01$; and 20 mg/kg: $P < 0.001$). Notably, the inhibitory capacity of M-NMs at a dose of 20 mg/kg was comparable with the positive control namely dexamethasone (DXMS). Furthermore, M-NMs exhibited significantly greater inhibition of edema compared to ei-

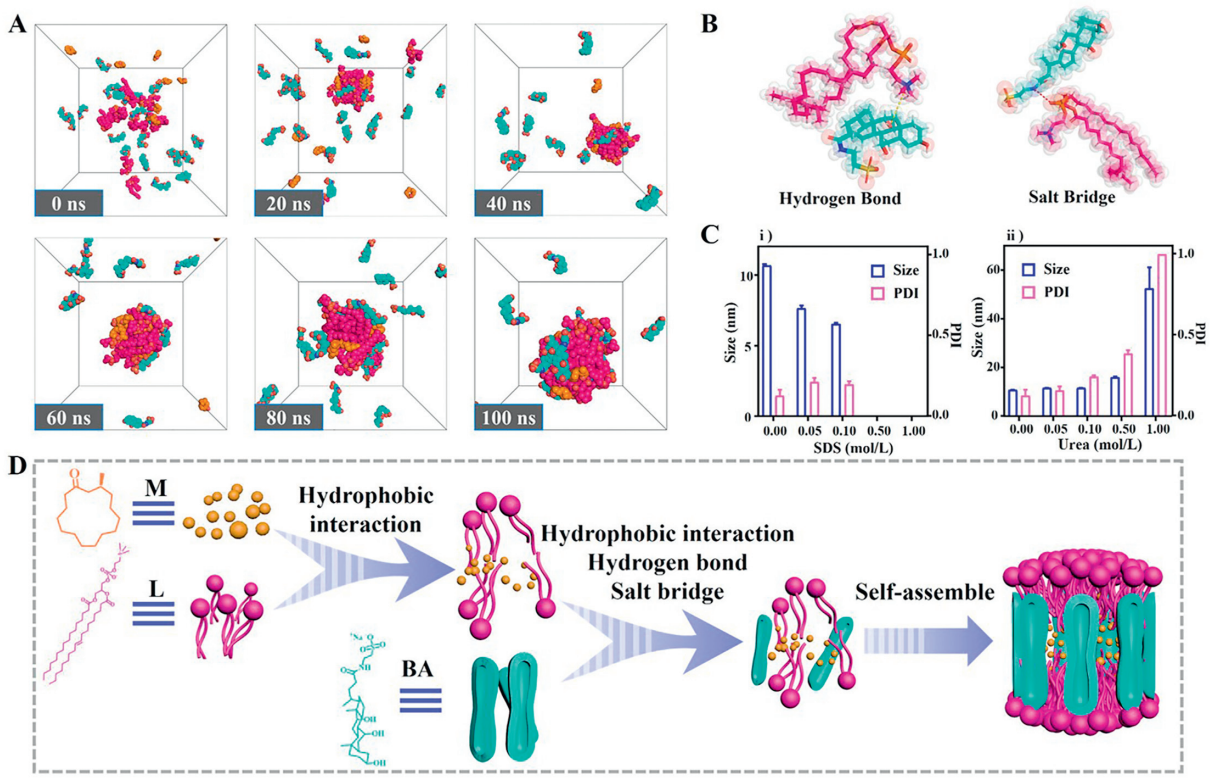


Fig. 4. The self-assembly mechanism of M-NMs. (A) Spontaneous aggregation of a random solution of TCA, POPC, and Muscone into mixed micelles. TCA are shown in green except for the hydroxyl groups (red), POPC in light pink, and M in orange. (B) Intermolecular interactions in M-NMs featuring hydrogen bonding and salt bridges. (C) Variations of hydrodynamic sizes and PDI of M-NMs with the addition of SDS (i) and urea (ii). (D) The mechanism underlying the self-assembly of M-NMs. Hydrophobic interaction, hydrogen bonding, and salt bridge are revealed as the primary correlations amongst taurocholic acid, lecithin, and muscone.

ther M-Tween-80 solution or BA-L NMs, particularly at high dose ($P < 0.05$), although the latter two also displayed significant anti-inflammatory activities (Fig. S18). The histopathological assay results of mouse ears are shown in Fig. S19 (Supporting information). In the control group, normal morphology and structure were observed in the ear tissues; however, inflammatory cell infiltration and edema were evident in the model group. On the other side, treatments with M-Tween-80 solution and BA-L NMs at high doses merely showed moderate pharmacological effects. Fortunately, following the M-NMs treatment, both cell infiltration and ear edema were dramatically alleviated in a dose-dependent manner.

We also evaluated the anti-inflammatory effects of M-NMs on acute carrageenan-induced inflammation rats through monitoring the changes in the perimeter of the right hind paw (Fig. S20A in Supporting information). Following subcutaneous injection of 1 % carrageenan into the right hind paw, there was a gradual increase in paw perimeter against time, arriving at the maximal value at approximately 2 h. All groups receiving medication administration and dexamethasone group that served as the positive control, exhibited the reduced swelling in comparison to the model group. Rats were sacrificed after 3 h for further assays. We measured the weight of rats' hind paws to validate our findings (Fig. S20B in Supporting information). Although M-NMs demonstrated a suppressive effect on paw swelling, the results lacked statistical significance. This may be attributed to inherent variations within the experimental groups and limited penetration through the thick stratum corneum of paw skin.

Thereafter, we employed specific markers in serum to further justify these findings and elucidate the underlying mechanisms in response to the anti-inflammatory benefits. The anti-inflammatory effects of the M-NMs were assessed through assaying NO and PGE_2 production. As illustrated in Fig. 5A, NO production in the xylene-induced model group was approximately three times higher than that of the control group ($P < 0.01$). However, a dose-dependent reduction in NO production occurred in M-NMs groups (10, 15, and 20 mg/kg). At the highest concentration level, NO production level was almost comparable with dexamethasone (DXMS). Additionally, both M-Tween-80 solution and BA-L NMs groups also suppressed NO production; however, statistical significance was absent. Similar results were observed for PGE_2 production as well (Fig. 5A). In response to exogenous stimulation, theoretically, the activated macrophages orchestrate a cascade of inflammatory processes by upregulating the activity of inducible nitric oxide synthase (iNOS) enzymes for continuous synthesis and release of substantial amounts of NO Additionally, PGE_2, generated by the inducible isoform cyclooxygenase-2 (COX-2), served as a potent inflammation mediator. Therefore, modulating the expression levels of iNOS and COX-2 to maintain physiological levels of NO and PGE_2 represented a promising therapeutic strategy for mitigating inflammatory conditions [46]. Exactly, our findings demonstrated that M-NMs effectively attenuated NO and PGE_2 production in xylene-induced mice ear swelling models.

The inhibitory effects of M-NMs on the expression of proinflammatory cytokines, including TNF-α, IL-1β, and IL-6, were investigated using ELISA assays. Fig. 5A indicates that xylene stimulation significantly increases the production of all proinflammatory cytokines when comparing with the control group. However, M-NMs treatment remarkably inhibited the xylene-induced increment in these cytokines in a dose-dependent manner. At the highest concentration level, M-NMs exhibited the greatest inhibitory effect on cytokine production, which was significantly superior to both M-Tween-80 and BA-L NMs groups ($P < 0.01$). These findings

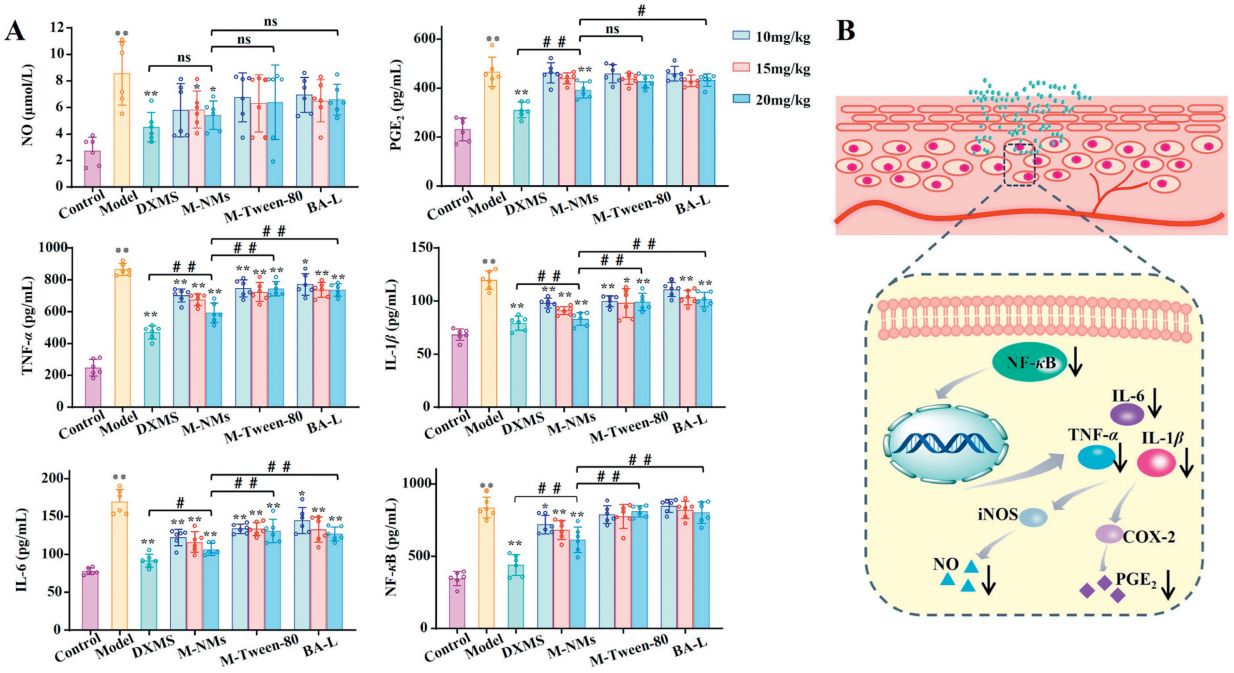


Fig. 5. Anti-inflammatory effects of M-NMs. (A) Measurement of serum NO levels in mice using the Griess Reagent and ELISA assays for determinations of PGE_2, TNF-α, IL-1β, IL-6, and NF-κB. $^{**}P < 0.05$ *vs.* control group, $^{*}P < 0.05$, $^{**}P < 0.01$, $^{***}P < 0.001$ *vs.* model group. $^{\#}P < 0.05$, $^{\#\#}P < 0.01$ *vs.* M-NMs high dose group, ns: no significance. (B) Schematic illustration of the dermal delivery process and the anti-inflammatory mechanism of M-NMs.

suggested that M-NMs exerted an anti-inflammatory effect by regulating the expression of proinflammatory cytokines.

Proinflammatory cytokines, such as TNF-α, which are primarily produced by macrophages and mast cells, serve as one of the earliest and most crucial inflammatory mediators. They induce the expressions of iNOS and COX-2, leading to the production of NO and PGE_2 in turn [47]. While these proinflammatory cytokines activate numerous signaling pathways, it is widely acknowledged that NF-κB group of transcription factors plays a determinant role in inflammation [48]. Activation of NF-κB up-regulates the expression of proinflammatory cytokine genes including TNF-α, IL-1β, and IL-6 [49]. ELISA assays demonstrated a reduction in NF-κB levels following M-NMs treatment (Fig. 5A). Above all, the anti-inflammatory effects of M-NMs mainly relied on the regulation of NF-κB signaling pathway [50,51], and the signaling pathway is summarized in Fig. 5B.

The anti-inflammatory effects of M-NMs were significantly strengthened when comparing with M-Tween-80 group in both RAW 264.7 cell experiments and dermal delivery. The improved anti-inflammatory effects of M-NMs on cells could be attributed to their exceptional stability in DMEM. Hence, our attention was forwarded to investigate the enhanced dermal delivery mechanisms of M-NMs. Initially, we compared the particle size between M-NMs and M-Tween-80 solution. The particle size of M-Tween-80 solution was approximately 200–300 nm, significantly greater than that of M-NMs (Fig. S21A in Supporting information). This smaller size of M-NMs exactly increased the contact area between the skin and muscone, further enhancing the penetration across the skin. Consequently, skin permeation studies were conducted for both M-NMs and M-Tween-80 solution. As shown in Fig. S21B (Supporting information), the permeation across the skin is continuous and roughly follows a first-order kinetic model: $Q_n = 3.9366t + 11.372$ ($R^2 = 0.9847$) for M-NMs, and $Q_n = 3.0055t + 1.5831$ ($R^2 = 0.9981$) for M-Tween-80 solution. M-NMs advanced muscone delivery crossing the skin and significantly enhanced its permeation compared to M-Tween-80 solution, which exhibited a cumulative permeation of 61.07 μg/cm^2 after a 12-h incubation, significantly higher than M-Tween-80 solution group (38.07 μg/cm^2). This could be attributed to the small size of M-NMs facilitating their penetration across the skin surface and their lipophilic nature promoting retention within the skin tissues [52]. As a result, the enhanced anti-inflammatory effects of M-NMs demonstrated their potential as a promising clinical agent for dermal administration. Transdermal drug delivery involves a complex process where factors beyond particle size, including flexibility, surface charge, and hydrophobicity, significantly influence permeation. Additionally, the penetration pathways of nanomicelles (intracellular, intercellular, follicular) warrant further investigation [44,53].

The biosafety of drugs is crucial for the clinical applications. In order to assess the safety of M-NMs at the prerequisite of ideal anti-inflammatory performances, we preliminarily conducted cytotoxicity assays. Cell Counting Kit-8 (CCK-8) assay was employed to evaluate *in vitro* cytotoxicity of M-NMs, M-Tween-80, and BA-L NMs using RAW 264.7 cells. Following 24-h incubation at concentrations being lower than 60 μmol/L, all inhibition rates of M-NMs, M-Tween-80, and BA-L NMs on RAW 264.7 cells were <10% (Fig. S22 in Supporting information), indicating their favorable biosafety properties. However, when the concentrations were greater than 80 μmol/L, M-NMs exhibited a higher inhibition rate possibly attributing to muscone-induced cytotoxicity, whereas BA-L NMs displayed excellent biosafety even at a concentration as great as 100 μmol/L. Notably, compared to M-Tween-80 solution, the significantly greater cytotoxicity observed for M-NMs at 100 μmol/L may attribute to the enhanced stability of M-NMs in DMEM (Fig. 2H). Skin safety assessments including skin irritation, skin sensitization, and photo-toxicity demonstrated favorable dermal biocompatibility of muscone [54]. Actually, transdermal anti-inflammatory experiments also confirmed that M-NMs did not induce significant redness, swelling, or allergic reactions, suggesting their suitability for transdermal delivery. Further investigations should prioritize comprehensive safety assessments of M-

NMs, including detailed toxicological profiling and dose-response analyses.

In summary, we developed 96wp mediated method to screen host-guest complexes, which owned high-throughput, cost-effective, and user-friendly advantages. The developed approach successfully enabled rapid screening of 51 natural products towards the guest molecule for the biomimetic nanocarrier namely BA-L NMs. As a result, BA-L NMs demonstrated significant potential towards facilitating the delivery of natural products, particularly muscone and chalcones. Because of the outstanding pharmacological property, muscone was implemented as the guest molecule of choice for BA-L NMs. After careful formula optimization, the prepared M-NMs exhibited exceptional stability and dramatically advanced the solubility of muscone in hydrophilic medium. Diverse spectroscopic and spectrometric assays and MD simulations revealed that hydrophobic interactions, hydrogen bonds, and salt bridges jointly governed the self-assembly and stability of M-NMs. Due to the nanomicelle features, M-NMs demonstrated excellent dermal delivery properties along with enhanced anti-inflammatory effects on cells and skins, attributing to the significant exposure improvement of muscone. Future investigations should prioritize elucidating the mechanism of action, conducting comprehensive safety assessments, and investigating detailed transdermal delivery mechanisms of M-NMs. Above all, 96wp mediated strategy is versatile for host-guest molecule screening, accelerating the development of natural product nanomicelles.

Ethics approval and consent to participate

All the animal experiments were conducted in accordance with the Animal Research Ethics Principles of Beijing University of Chinese Medicine (Approval numbers: BUCM-2023091901-3146 and BUCM-2023100802-4004).

Declaration of competing interest

The authors declare that they have no known competing financial interests or personal relationships that could have appeared to influence the work reported in this paper.

CRediT authorship contribution statement

Wenzheng Li: Conceptualization, Writing – original draft, Methodology. **Ke Zhang:** Methodology, Investigation. **Wenjing Liu:** Formal analysis. **Ting Li:** Investigation. **Wei Li:** Visualization. **Lijuan Wu:** Investigation. **Maodong Wang:** Investigation. **Hangyun He:** Investigation. **Pengfei Tu:** Supervision, Writing – review & editing. **Yuelin Song:** Writing – review & editing, Funding acquisition, Project administration.

Acknowledgments

This study was financially supported by the National Natural Science Foundation of China (Nos. 82474202 and 81973444).

Supplementary materials

Supplementary material associated with this article can be found, in the online version, at doi:10.1016/j.cclet.2025.111548.

References

[1] Y.H. Qiao, Z.H. Wei, T.T. Qin, et al., Chin. Chem. Lett. 32 (2021) 2877–2881.
[2] Y.Z. Tan, Z.K. Guo, M.Y. Zhu, et al., Chin. Chem. Lett. 31 (2020) 1406–1409.
[3] X. Guo, W. Luo, L. Wu, et al., Adv. Sci. 11 (2024) 2403388.
[4] M. Abdulkarim, P.K. Sharma, M. Gumbleton, Adv. Drug Deliv. Rev. 142 (2019) 62–74.
[5] R. Garriga, I. Jurewicz, E. Romero, et al., ACS Appl. Mater. Interfaces 8 (2016) 1913–1921.
[6] Y. Lu, Z. Yue, J. Xie, et al., Nat. Biomed. Eng. 2 (2018) 318–325.
[7] Y. Liu, L. Shi, L. Su, et al., Chem. Soc. Rev. 48 (2019) 428–446.
[8] Y. Hui, X. Yi, F. Hou, et al., ACS Nano 13 (2019) 7410–7424.
[9] M.J. Mitchell, M.M. Billingsley, R.M. Haley, et al., Nat. Rev. Drug Discov. 20 (2021) 101–124.
[10] A. Barone, M.C. Cristiano, F. Cilurzo, et al., Colloids Surf. B: Biointerfaces 193 (2020) 111152.
[11] J. Schlauersbach, J. Kehrein, S. Hanio, et al., Mol. Pharmaceutics. 19 (2022) 2868–2876.
[12] C. López-Sánchez, F. de Andrés, M. Zougagh, et al., Anal. Chim. Acta 1348 (2025) 343820.
[13] J. Fan, H. Yu, X. Lu, et al., ACS Appl. Mater. Interfaces 15 (2023) 8854–8871.
[14] W. Liu, H.S. Jayasekera, J.D. Sanders, et al., Anal. Chem. 95 (2023) 17212–17219.
[15] D. Wu, H. Tang, X. Qiu, et al., Nat. Protoc. 20 (2025) 1–25.
[16] V. Agrahari, Y.E. Choonara, M. Mosharraf, S.K. Patel, F. Zhang, Pharm. Res. 41 (2024) 2289–2297.
[17] X.Y. Zhu, Y. Li, N. Gu, Nano Biomed. Eng. 15 (2023) 342–353.
[18] S.T. Jones, Z. Walsh-Korb, S.J. Barrow, et al., ACS Nano 10 (2016) 3158–3165.
[19] S.S. Mishra, S. Mohanty, J. Mishra, U. Subuddhi, Langmuir 35 (2019) 16555–16567.
[20] P. Sharma, N. Sohal, B. Maity, RSC Adv. 11 (2021) 10912–10921.
[21] L.Y. Zhou, M. Yao, Z.R. Tian, et al., J. Neurochem. 155 (2020) 154–176.
[22] J. Wang, H. Xing, X. Qin, et al., J. Ethnopharmacol. 262 (2020) 113120.
[23] G. Ottaviani, D.J. Gosling, C. Patissier, et al., Eur. J. Pharm. Sci. 41 (2010) 452–457.
[24] A. Michałowska, O. Kupczyk, A. Czyrski, Pharmaceutics 15 (2023) 1774.
[25] N.A. Malik, Appl. Biochem. Biotechnol. 179 (2016) 179–201.
[26] J. Zheng, R. Fan, H. Wu, et al., Nat. Commun. 10 (2019) 1604.
[27] X. Zhang, Y. Huang, H. Song, et al., J. Control. Release 328 (2020) 454–469.
[28] S. Hanio, J. Schlauersbach, B. Lenz, et al., Langmuir 37 (2021) 2543–2551.
[29] J. Wiest, M. Saedtler, B. Böttcher, et al., Mol. Pharm. 15 (2018) 4470–4480.
[30] K. Müller, Biochemistry 20 (1981) 404–414.
[31] M.C. Carey, Hepatology 4 (1984) 138S–142S.
[32] D. Madenci, A. Salonen, P. Schurtenberger, et al., Phys. Chem. Chem. Phys. 13 (2011) 3171–3178.
[33] Y. Li, J. Liu, Y. Wang, et al., Anal. Chem. 87 (2015) 7958–7963.
[34] H.F. Su, L. Xue, Y.H. Li, et al., J. Am. Chem. Soc. 135 (2013) 6122–6129.
[35] G. Siuzdak, B. Bothner, Angew. Chem. Int. Ed. 34 (1995) 2053–2055.
[36] K. Zhang, J. Jia, T. Li, et al., Acta Pharm. Sin. B 14 (2024) 4045–4058.
[37] T. Kundlacz, C. Schmidt, Anal. Chem. 95 (2023) 17292–17299.
[38] C.V. Robinson, E.W. Chung, B.B. Kragelund, et al., J. Am. Chem. Soc. 118 (1996) 8646–8653.
[39] M.A. Hammad, B.W. Müller, Eur. J. Pharm. Biopharm. 46 (1998) 361–367.
[40] H.R. Jia, Y.X. Zhu, K.F. Xu, et al., Adv. Healthc. Mater. 7 (2018) e1800380.
[41] G. Graciani, J.T. King, F. Amblard, ACS Nano 16 (2022) 16796–16805.
[42] Q.Q. Liang, M. Zhang, Q. Zhou, et al., Clin. Orthop. Relat. Res. 468 (2010) 1600–1610.
[43] Y. Yang, J. He, Y. Suo, et al., Biomed. Pharmacother. 81 (2016) 424–430.
[44] N. Tiwari, E.R. Osorio-Blanco, A. Sonzogni, et al., Angew. Chem. Int. Ed. 61 (2022) e202107960.
[45] H. Gao, X. Liu, W. Sun, et al., Cell Death. Dis. 8 (2017) e3004.
[46] Z. Zhang, S. Jiang, H. Tian, et al., J. Ethnopharmacol. 269 (2021) 113698.
[47] H. Zhao, L. Wu, G. Yan, et al., Signal Transduct. Target Ther. 6 (2021) 263.
[48] Q. Li, I.M. Verma, Nat. Rev. Immunol. 2 (2002) 725–734.
[49] G. Andonegui, C.S. Bonder, F. Green, et al., J. Clin. Invest. 111 (2003) 1011–1020.
[50] S. Lv, Z. Lei, G. Yan, et al., J. Ethnopharmacol. 284 (2022) 114799.
[51] K. Liu, L. Xie, M. Deng, et al., Chin. Med. 16 (2021) 46.
[52] H. Joshi, A.R. Hegde, P.K. Shetty, et al., Photodermatol. Photoimmunol. Photomed. 34 (2018) 69–81.
[53] X. Chen, Adv. Drug Deliv. Rev. 127 (2018) 85–105.
[54] D. McGinty, C.S. Letizia, A.M. Api, Food Chem. Toxicol. 49 (2011) S120–S125.